NJC

Accepted Manuscript

Volume 40 | Number 1 | January 2016 | Pages 1–846

NJC

New Journal of Chemistry
www.rsc.org/njc

A journal for new directions in chemistry

ISSN 1144-0546

ROYAL SOCIETY OF CHEMISTRY

PAPER
Jason B. Benedict et al
The role of atropisomers on the photo-reactivity and fatigue of
diarylethene-based metal–organic frameworks

cnrs

ROYAL SOCIETY OF CHEMISTRY

rsc.li/njc

Water insertion and combined interstitial-vacancy oxygen conduction in the layered perovskites La$_{1.2}$Sr$_{0.8-x}$Ba$_x$InO$_{4+\delta}$

L. Troncoso[a],* M.D. Arce[b], M.T. Fernández-Díaz[c] , L.V. Mogni[b], J.A. Alonso[d]

a Instituto de Materiales y Procesos Termomecánicos, Universidad Austral de Chile, General Lagos, 2086, 5111187, Valdivia, Chile
b CNEA-CONICET, Centro Atómico Bariloche, Av. Bustillo 9500, S. C. de Bariloche, Río Negro, 8400, Argentina
c Institut Laue-Langevin, B.P. 156, F-38042 Grenoble Cedex 9, France
d Instituto de Ciencia de Materiales de Madrid, CSIC, Cantoblanco, 28049 Madrid, Spain

Abstract

Layered perovskites of K$_2$NiF$_4$-type consist of single octahedral sheets alternating with NaCl-type layers, containing a substantial interstitial space. Based on the parent LaSrInO$_{4+\delta}$ oxide, the series of title compounds have been prepared and investigated as possible solid electrolytes for solid-oxide fuel cells (SOFC). A charge misbalance is created by departure from the La/Sr=1:1 ratio, favoring the insertion of extra oxygen atoms. The oxygen diffusion is further favored by introducing large Ba^{2+} ions, expanding the unit-cell size. Surprisingly, the presence of basic Ba ions drives the spontaneous insertion of water molecules in the interstitial space, as unveiled by a neutron powder diffraction (NPD) study at RT. Moreover, H$_2$O molecules are split within the structure with protons bonded to the axial oxygens of the InO$_6$ octahedra, and with OH units occupying the interstitial space. Electrical Conductivity measurements were made. The dc conductivity was measured under different oxygen partial pressures for both Ba-doped compounds at 600 °C and 800 °C showing mixed ionic and p-type electronic behavior at different oxygen partial pressures but with conductivities of the order of ≈10^{-4} (S/cm), far below the conductivities values of the oxide electrodes used in SOFCs. To analyze the nature of the majority charge carrier, ac impedance spectroscopy (IS) was applied. In the temperature range 500–900 °C, La$_{1.2}$Sr$_{0.6}$Ba$_{0.2}$InO$_{4+\delta}$ oxide exhibits a conductivity improvement with respect to La$_{1.2}$Sr$_{0.8}$InO$_{4+\delta}$. Temperature-dependent NPD data show at 600ºC and 800ºC the presence of oxygen vacancies at the axial octahedral positions as well as interstitial oxygen, favoring a mixed conduction mechanism for oxide ions, which may account for the enhancement of the transport properties. The present result

New Journal of Chemistry Accepted Manuscript

endorses the validity of this design procedure and supports K_2NiF_4-related compounds as promising candidates for solid-oxide electrolytes.

Keywords: Layered perovskite; interstitial oxygen atoms; water splitting; solid electrolyte
*Corresponding author. E-mail: Loreto.troncoso@uach.cl

1. Introduction

Energy conversion devices such as solid oxide fuel cells (SOFCs) are an excellent alternative for stationary applications, since they are ideal for out-of-grid energy conversion devices in areas where the installation of power lines is not possible. On the other hand, the heat produced during its operation can be used to provide hot water or heating [1][2]. Unfortunately, the working temperatures for SOFC devices are too high, being around 1000 °C. This is because the electrolyte, which is a conductor of oxide ions, needs high temperatures to activate the oxygen motion. For this reason, it is essential to find alternative oxide-ion conducting materials with low activation energies and low resistance, to permit lowering the working temperatures to intermediate values (600 – 850°C), but without undermining the performance of SOFCs; that is to say, without harming the electrochemical kinetics of the device. An ionic conductor is obtained by generating charge imbalances inside the crystalline structure, driving the creation of point defects in the network such as vacancies and/or interstitials. The most studied compounds that have shown an excellent performance are those based on the fluorite compositions of YSZ[3], GDC[4] and the perovskite-type LSGM[5]; the diffusion mechanism of these three ion-conducting materials is based on the creation of oxygen vacancies in the network. All exhibit oxygen ion conductivity values of $\sigma \geq 0.10$ S/cm between 700 and 1000 °C. There are also new alternatives under study for crystalline structures such as apatites[6], and perovskites of the Ruddlesden-Popper type, which allow the introduction of interstitial oxygens inside their structure. The perovskites in layers of K_2NiF_4 type are well known for their ability to incorporate a substantial number of interstitial oxygens in their framework[7-12]. The atomic arrangement A_2BO_4 is constituted by BO_6 octahedra sharing vertices in a single perovskite layer, which alternates with a NaCl-type structure of AO layers. There are two types of oxygen atoms; equatorial O1 oxygens,

corner-connecting the BO_6 octahedra in the basal plane, while O2 axial oxygens link the perovskite layer with the NaCl–type layer. The interstitial atoms, responsible for the O^{2-} diffusion, are located in the sodium chloride-type layer, only coordinated by A cations [13].

In previous investigations on layered perovskites with K_2NiF_4 structure, we described $LaSrInO_{4+\delta}$ derivatives [14][15] as promising electrolytes with oxide-ion conductivity. The series of compounds $LaSrIn_{1-x}B_xO_{4+\delta}$ (B=Zr, Ti, x= 0.1, 0.2) and $La_{1+x}Sr_{1-x}InO_{4+d}$ (x= 0.1, 0.2) were characterized by neutron diffraction and its capability of incorporating interstitial oxygen atoms (δ) was identified. The best results were found for $La_{1.2}Sr_{0.8}InO_{4+\delta}$ describing the lowest resistivity and more labile oxygens, which was consistent with the higher quantity of interstitial oxygen atoms found from neutron powder diffraction (NPD) data (δ= 0.11(1)).

Based on these previous studies, we propose the partial replacement of Sr cations for larger Ba^{2+} ions in the $La_{1.2}Sr_{0.8-x}Ba_xInO_{4+\delta}$ (x= 0.2, 0.3) series. It is expected that the oxygen diffusion will be further favored upon the expansion of the unit-cell size. The materials characterization includes the evaluation of the AC electrical conductivity and a neutron diffraction study, useful to locate the positions and determine the occupation of the interstitial oxygen atoms. Additionally, $La_{1.2}Sr_{0.6}Ba_{0.2}InO_{4+\delta}$ demonstrated to have a double functionality, since at RT it is able to absorb and split water into the interlayer space, probably due to the basic character of Ba ions, as demonstrated from the NPD study.

2. Experimental

$La_{1.2}Sr_{0.8-x}Ba_xInO_{4+\delta}$ (x= 0.2, 0.3) oxides were prepared via a nitrate–citrate route. Stoichiometric amounts of analytical grade $Sr(NO_3)_2$, $La(NO_3)_3 \cdot 6HO$, $Ba(NO_3)_2$ and $In(NO_3)_3 \cdot 9H_2O$ were dissolved under stirring in 250 mL of 10% citric-acid aqueous solution with several droplets of concentrated HNO_3. This mixture was slowly evaporated, leading to organic resins where a random distribution of the involved cations is obtained. The resins were dried at 120 °C and slowly decomposed at temperatures up to 600 °C. A subsequent treatment at 800 °C for 2 h ensures the total elimination of all the organic materials and nitrates. A heating at 1000 °C for 12 h gave rise to well-crystallized, homogeneous samples. The products underwent a final treatment at 1300ºC to ensure that the consolidated crystal

structure is similar to that of the samples studied by transport techniques. The identification and characterization of the final products to assess phase purity were carried out by X-ray diffraction (XRD) using a Bruker-axs D8 diffractometer (40 kV, 30 mA), controlled by DIFFRACTplus software, in the Bragg–Brentano reflection geometry with CuKα radiation (λ= 1.5418 Å). Neutron powder diffraction (NPD) data were collected in the D2B diffractometer at the Institut Laue-Langevin, Grenoble, in the high-resolution configuration with a neutron wavelength λ = 1.549 Å. About 2 g of the sample was contained in a vanadium can and placed in the isothermal zone of a furnace with a vanadium resistor operating under vacuum ($PO_2 \approx 10^{-6}$ Torr). The measurements were carried out at 25ºC (RT), 600 and 800°C for the selected $La_{1.2}Sr_{0.6}Ba_{0.4}InO_{4+\delta}$ composition. The counting time for each pattern was 2 h. The crystal structures were analyzed by the Rietveld method [16], using the FULLPROF refinement program [17]. The peak profiles were modeled by a pseudo-Voigt function. The following parameters were refined in the final runs: scale factor, background coefficients, zero-point error, pseudo-Voigt corrected for asymmetry parameters, unit-cell parameters, and positional, isotropic thermal factors for the metals and anisotropic for O1 and O2 oxygen atoms. Occupancy factors for oxygen atoms were also refined for NPD data. The coherent scattering lengths for La, Sr, In, Ba and O were 8.240, 7.020, 4.065, 5.070 and 5.803 fm, respectively.

For electrical conductivity measurements, dense compounds are required. The prepared powders were pressed into pellets (7mm in diameter and 1.4 mm thick) at 200 MPa for 5 min to form a green pellet. Then, these pellets were sintered in air at 1300 °C for 12 h. The final densities were in the range of 90–95%. Both sides of the pellets were painted with Pt paste, as current collectors, and fired at 800 °C for 1 hour. AC conductivity was obtained by impedance spectroscopy. All the impedance measurements were performed in the 600–900 °C temperature range in air atmosphere. The impedance spectra were collected in an AUTOLAB system (PGSTAT30 and FRA2 module) from Eco Chemie B.V. The measurements were performed from 1 MHz to 100 mHz at open circuit using two electrode configurations with a signal amplitude of 50 mV. The experimental data were adjusted with the Zview program [18]. 2-probe DC conductivity measurements were perform on dense bars using Pt as current collector. Conductivity values were acquired with an Agilent 34972A

Data Adquisition Unit at a temperature range between RT and 800 ºC under atmospheric air. At 600 and 800 ºC the conductivity response was evaluated as a function of oxygen partial pressure (pO$_2$) between ~ 5.10^{-21} and 1 atm. The pO$_2$ was controlled and sensed through an electrochemical gas blending system, which consisted on a zirconia pump and oxygen sensor, coupled to the 2-probe conductivity system [19].

Thermogravimetric (TG) analysis was performed using a Cahn 1000 electrobalance [19] by cycling the sample between RT and 800 ºC under dry synthetic air. The total reduction of the sample was performed at 800 ºC under 100% H$_2$ atmosphere till no further mass weight loss was detected, even at higher temperatures or H$_2$ flux.

3. Results and discussion

3.1 Crystallographic characterization

La$_{1.2}$Sr$_{0.8-x}$Ba$_x$InO$_{4+\delta}$ (x= 0, 0.2, 0.3) oxides were obtained as well-crystallized powders. Fig. 1 shows the XRD patterns, which are characteristic of K$_2$NiF$_4$ phases, with superstructure peaks indicating a deviation of the tetragonal *I4/mmm* structure.
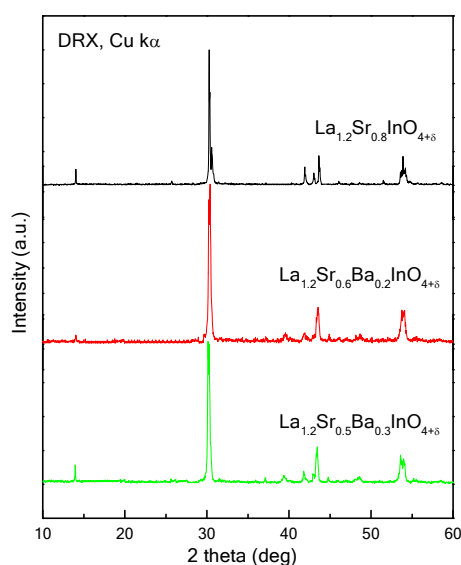

Figure 1. XRD patterns of the materials of the series La$_{1.2}$Sr$_{0.8-x}$Ba$_x$InO$_{4+\delta}$, collected with Cu K$_\alpha$ radiation.

All the patterns could be indexed in an orthorhombic symmetry. The unit-cell parameters and volume at RT for the three materials are listed in Table 1. A progressive expansion of the unit-cell volume is observed as Ba content increases, as expected. This is a result of the regular increase of b and c parameters, although a presents a non-monotonic behavior.

Table 1. Unit-cell parameters and volume at RT for $La_{1.2}Sr_{0.8-x}Ba_xInO_4$

x	0	0.2	0.3
$a(Å)$	12.6085(6)	12.586(1)	12.609(1)
$b(Å)$	5.8789(3)	5.9092(2)	5.9194(7)
$c(Å)$	5.8338(3)	5.8453(7)	5.8563(7)
$V(Å^3)$	432.42(4)	434.72(8)	437.12(9)

A neutron powder diffraction (NPD) study at room and high temperature was essential to investigate the structural details concerning the location of interstitial oxygen atoms. The crystal structure of $La_{1.2}Sr_{0.6}Ba_{0.2}InO_{4+\delta}$ was first refined at RT from NPD data in the Pbca space group (No 61) as proposed by Titov [20] for the nominal composition $LaSrInO_4$. In the Pbca model, La, Sr and Ba atoms are located at random at 8c (x,y,z) positions; In is placed at 4b (1/2,0,0) sites and the two types of oxygen atoms O1 and O2 are also at 8c sites.

The presence of vacancies at the octahedral lattice at RT was discarded, since the occupancy factors of O1 and O2 atoms yielded full stoichiometry for both positions. Interstitial O3 oxygen atoms were first placed at 8c Wyckoff sites with x≈y≈z≈0.25 positions and located at the NaCl layers. For $La_{1.2}Sr_{0.6}Ba_{0.2}InO_{4+\delta}$ the value of delta required for electroneutrality is $\delta=0.1$; however the initial refinements yielded the significantly higher value of $\delta=0.6$ for the interstitial atoms. This is unreasonable since the metal elements cannot vary their oxidation states from the nominal 3+ for La and In and 2+ for Sr and Ba. A difference Fourier map conspicuously showed negative peaks in the interlayer region (NaCl layers) corresponding to hydrogen atoms (Fig. 2), of two independent crystallographic types.
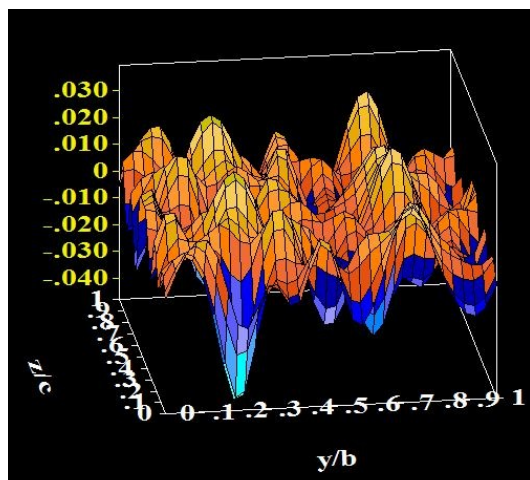
Figure 2. Localization of the interstitial hydrogen atoms (H2) in $La_{1.2}Sr_{0.6}Ba_{0.2}InO_{4+\delta}$ by difference Fourier analysis, corresponding to the x= 0.344 layer, from NPD data at RT.

The introduction of these atoms and the refinement of the occupancy factors and atomic positions gave a significant water content of about 0.50 molecules per formula unit. A reduction of the R_{Bragg} from 9% to 7% was observed after the inclusion of H1 and H2 into the structural model. Table 2 lists the atomic parameters after the full refinement of the structure and Table 3 includes the anisotropic displacement factors for O1 and O2 (ADP); Table 4 contains the main bond distances and angles at RT.

Table 2. Structural parameters and discrepancy factors after the Rietveld refinement of $La_{1.2}Sr_{0.6}Ba_{0.2}InO_{4+\delta}$ in the space group P*bca* from NPD data at increasing temperatures.

T(ºC)	25	600	800
a(Å)	12.586(1)	12.720(1)	12.776(1)
b(Å)	5.9092(2)	5.9240(4)	5.9257(4)
c(Å)	5.8453(7)	5.8651(5)	5.8756(5)
V(Å³)	434.72(8)	441.96(6)	444.81(6)
La/Sr/Ba 8*c*			
(x,y,z)			
x	0.1466(1)	0.1469(1)	0.1457(1)
y	-0.0240(4)	-0.0067(4)	-0.0021(5)
z	0.9910(8)	0.9998(15)	0.998(1)
B(Å²)	1.5(8)	2.7(1)	3.4(1)
focc	0.6/0.3/0.1	0.6/0.3/0.1	0.6/0.3/0.1
In 4*b* (1/2 0 0)			
B(Å²)	0.63(8)	0.76(6)	0.89(1)
O1 8*c*(x,y,z)			

x	0.0203(3)	0.0217(3)	0.0222(3)
y	0.238(1)	0.2662(9)	0.252(1)
z	0.2280(6)	0.2742(7)	0.2273(7)
O2 8c(x,y,z)			
x	0.3205(4)	0.3219(3)	0.3256(4)
y	0.0754(6)	0.0676(5)	0.0657(6)
z	0.023(2)	0.022(2)	0.015(2)
$focc$	1.00	0.898(7)	0.961(7)
O3 8c(x,y,z)			
x	0.243(1)	0.2282(7)	0.213(1)
y	0.178(3)	0.344(1)	0.298(2)
z	0.329(2)	0.241(2)	0.181(2)
$B(Å^2)$	2.9(9)	2.3(1)	0.9(2)
$focc$	0.280(3)	0.152(7)	0.089(7)
H1 8c(x,y,z)			
x	0.185	-	-
y	0.073	-	-
z	0.312	-	-
$focc$	0.230(3)	-	-
H2 8c(x,y,z)			
x	0.3451(3)	-	-
y	0.2587(7)	-	-
z	0.4203(4)	-	-
$focc$	0.230(3)	-	-
Discrepancy factors			
χ^2	1.62	1.80	1.57
$R_p(\%)$	1.92	1.80	1.74
$R_{wp}(\%)$	2.48	2.35	2.21
$R_{Bragg}(\%)$	6.94	9.76	9.91

Table 3. Anisotropic displacement factors for O1 and O2 in $La_{1.2}Sr_{0.6}Ba_{0.2}InO_{4+\delta}$ from NPD data at increasing temperatures.

$T(^oC)$	**25**	**600**	**800**
O1 8c(x,y,z)			
β_{11}	61(7)	73(5)	96(7)
β_{22}	163(26)	138(16)	124(16)
β_{33}	42(20)	176(21)	156(20)
β_{12}	97(16)	4(16)	-24(27)
β_{13}	53(12)	7(15)	39(17)
β_{23}	171(21)	109(20)	100(20)

O2 8c(x,y,z)

β_{11}	43(5)	55(5)	94(8)
β_{22}	19(20)	205(28)	295(33)
β_{33}	802(56)	558(39)	602(51)
β_{12}	-23(9)	-18(11)	25(15)
β_{13}	-157(22)	-83(33)	-140(30)
β_{23}	-48(40)	-128(66)	-208(50)

* Anisotropic Betas β x 10^{-4}

Table 4. Main interatomic distances (Å^2) and angles (°) for $La_{1+x}Sr_{1-x}In_{4+\delta}$ (x= 0.0, 0.1 and 0.2) determined from NPD data at RT.

T(°C)	25	600	800
La/Sr-O1	2.612(6)	2.550(8)	2.566(7)
La/Sr-O1	2.770(5)	2.887(7)	2.924(6)
La/Sr-O1	2.775(6)	2.731(8)	2.684(7)
La/Sr-O2	2.281(5)	2.274(5)	2.335(5)
La/Sr-O2	2.783(10)	2.929(14)	2.882(12)
La/Sr-O2	2.409(4)	2.556(4)	2.589(5)
La/Sr-O3	2.595(15)	2.695(11)	2.249(13)
La/Sr-O3	1.925(16)	3.059(11)	3.131(13)
La/Sr-O3	2.980(15)	2.262(12)	2.415(13)
La/Sr-O3	2.567(17)	2.109(12)	2.379(14)
In-O1 (x2)	2.061(6)	2.033(7)	2.044(6)
In-O1 (x2)	2.137(5)	2.179(6)	2.211(6)
In-O2 (x2)	2.307(5)	2.302(5)	2.264(5)
H1-O2	1.520(8)		
H1-O3	0.963(17)		
H2-O2	1.191(7)		
H2-O3	1.461(16)		
In-O1-In	164.0(2)	163.3(3)	163.8(2)

Fig. 3 illustrates the goodness of the fit from NPD data at RT. La_2O_3 was found as minor impurity and included in the refinement as second phase.
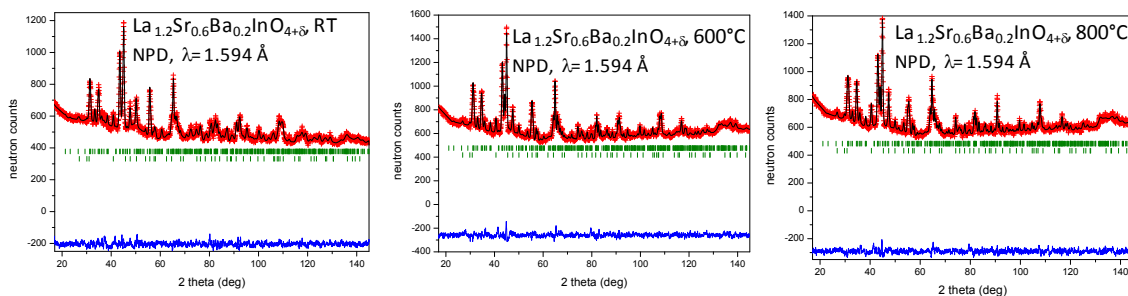
Figure 3. Observed (crosses), calculated (full line) and difference (at the bottom) NPD profiles for La$_{1.2}$Sr$_{0.6}$Ba$_{0.2}$O$_{4+\delta}$, at a) 25ºC, b) 600ºC and c) 800ºC, refined in the P*bca* space group. The vertical markers correspond to the allowed Bragg reflections for the main phase; the second series of markers correspond to La$_2$O$_3$ minor impurity phase.

As shown in Fig. 4a, the absorbed water molecules are dissociated after inclusion in the NaCl layers of this material, showing O-H bonds with the axial O2 atoms of the InO$_6$ octahedra and the interstitial O3 atoms. These details concerning dissociated water is highlighted in Fig. 4b. The O2-H and O3-H distances are close to 1 Å (see Table 4). Hydrogen bonds of about 1.5 Å (Table 4) are established in the interlayer space with O2 and O3 atoms.
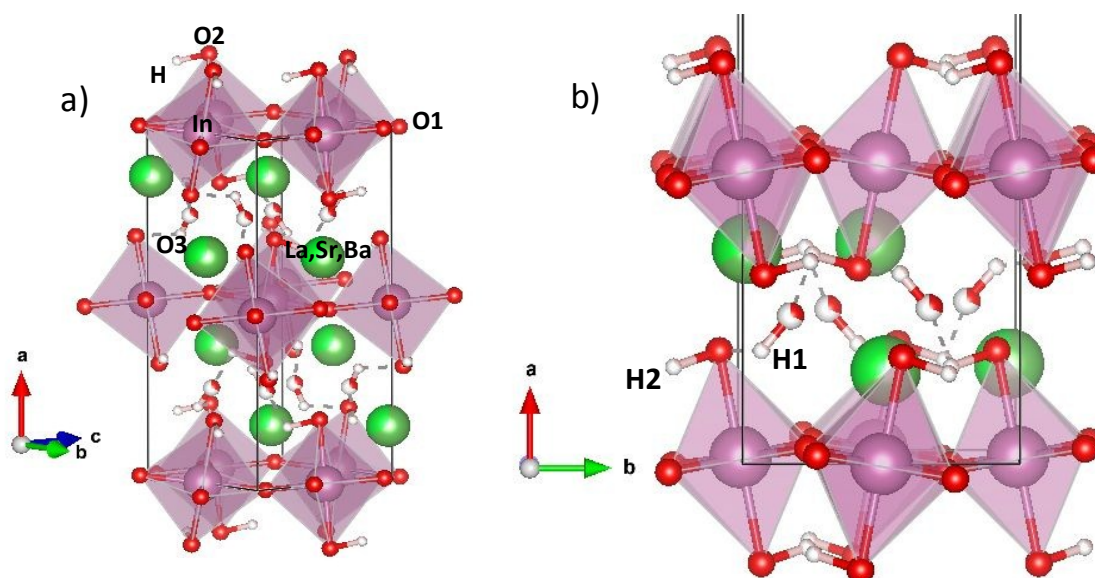

Figure 4. a) Crystal structure view of La$_{1.2}$Sr$_{0.6}$Ba$_{0.2}$O$_{4+\delta}$, showing sheets of tilted InO$_6$ octahedra alternating with (La,Sr,Ba)-O layers, where interstitial O3 oxygen atoms are located, as well as splitted water molecules. b) Close up image of the interstitial space where H1 is bonded to O3 interstitial oxygen atoms and H2 is bonded to O2 axial atoms of the InO$_6$ octahedra. Weaker hydrogen bonds are represented by dashed lines.

The crystal structures of the parent La$_{1.1}$Sr$_{0.9}$InO$_4$ and La$_{1.2}$Sr$_{0.8}$InO$_4$ oxides have been described in a former report [15], and the presence of interstitial oxygen atoms was unveiled from Fourier synthesis. However, in that case no water was detected in the interlayer space. In the present compounds, the introduction of the very basic Ba^{2+} ions, together with the calcination at 1300ºC, seems to give rise to materials with a strong affinity for water. This happens during the cooling process in the ambient laboratory conditions. Not only H$_2$O

molecules are introduced in the interplanar space (NaCl-type layers) but they are dissociated into O-H units; one of the H atoms per molecule is bonded to interstitial O3 atoms whereas the second one appears linked to the axial octahedral oxygen of the perovskite layers. Such water molecule dissociation has been described in some strongly oxygen-defective oxides, where H_2O molecules adopt the position of oxygen vacancies, releasing an H to be bonded to octahedral oxygens; this procedure is used for H_2 production since, upon heating the solid, the materials release H_2, whereas the O^{2-} ion fills the oxygen vacancy [21,22], for instance, in the $La_{0.6}Ca_{0.4}CoO_{3-\delta}$ perovskite. This has been described for 3D perovskites ($ABO_{3-\delta}$ type) but, to the best of our knowledge, it had not been reported for layered perovskites, with water inserted into the interstitial space.

Upon heating the present sample $La_{1.2}Sr_{0.8}Ba_{0.2}InO_{4+\delta}$ during an "in-situ" structural study, at 600ºC and 800ºC, the absorbed water is released and the refinement of the occupancy factor of the O3 interstitial atom becomes that expected ($\delta= 0.1$) for the charge misbalance produced upon introducing extra (Sr,Ba) with respect to the 1:1 La/(Sr,Ba) stoichiometry. Moreover, the neutron refinement shows the conspicuous appearance of oxygen vacancies in the axial O2 octahedral atoms; the refined stoichiometries at 600ºC and 800ºC are, respectively, $La_{1.2}Sr_{0.6}Ba_{0.2}In(O1)_2(O2)_{1.80(1)}(O3)_{0.30(1)}$ and $La_{1.2}Sr_{0.6}Ba_{0.2}In(O1)_2(O2)_{1.92(1)}(O3)_{0.18(1)}$. The total amount of oxygen at both temperatures is 4.10(1), as expected. There is no measureable oxygen deficiency on O1 positions. The presence of both O2 vacancies and O3 interstitials, both of them lying in the interlayer space, will have a strong influence in the transport properties, as we will show below.

On the other hand, the refinement of the anisotropic displacement factors (ADPs) for O1 and O2 atoms (belonging to the perovskite layers) yields strongly anisotropic ellipsoids for both atoms, as illustrated in Figure 5 for the structure at 600ºC.

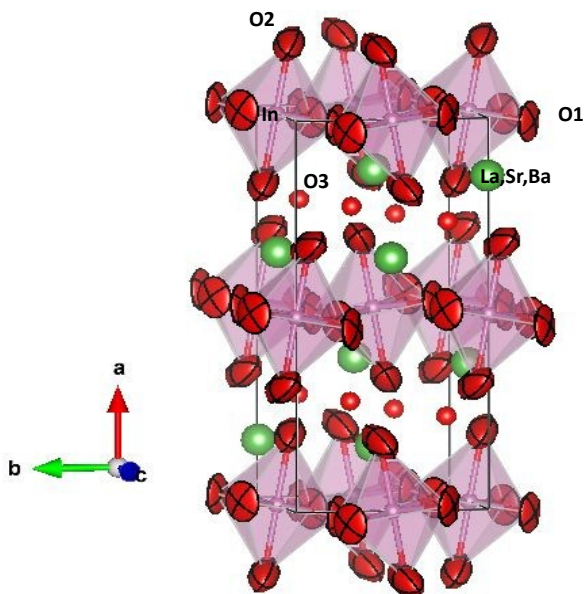**Figure 5**. View of the crystal structure of $La_{1.2}Sr_{0.6}Ba_{0.2}O_{4+\delta}$, highlighting the anisotropic displacement parameters, of oblate type for equatorial O1 and prolate type for axial O2 oxygen atoms. The ellipsoids are represented with 95% of probability.

Equatorial O1 oxygens are disk shaped (oblate-type) ellipsoids, which is the shape typically found in perovskites. They are perpendicular to the In-O-In bonds, where the thermal vibrations are preferentially oriented; i.e. these oblate spheroids lock the oxygen atoms at mid-indium positions with enhanced vibrations perpendicular to the In-In distance On the other hand, the ADPs for the axial oxygens are prolate-type, cigar-shaped ellipsoids, as illustrated in Fig. 5. In this case, the terminal oxygens of the octahedra are more ionically (weakly) bonded to the NaCl (La/Sr/Ba-O) counter-part of the crystal structure and, moreover, the direction of the long axis of the ellipsoid could mimic the oxygen exchange between the interstitial O3 atoms and the oxygen vacancies present in these octahedral positions, thus endorsing the oxide-ion diffusion across the solid.

3.2. Electrical Conductivity measurements

The dc conductivity measured under different oxygen partial pressures is shown in Fig. 6 for both Ba-doped compounds. At 600°C, as can be seen, the conductivities of both samples remain constant at very low oxygen partial pressure, but over 10^{-4} atm, mixed ionic and p-type electronic behavior is evidenced. To achieve partial pressures of oxygen of the order of

10^{-21} atm, it is necessary to make a mixture of gases with Ar, H_2 and water as buffer; therefore, to avoid damaging the platinum cables of the measuring device by embrittlement with hydrogen, at 800 °C we only performed measurements above 10^{-4} atm pO_2. In this case, the same trend is observed.
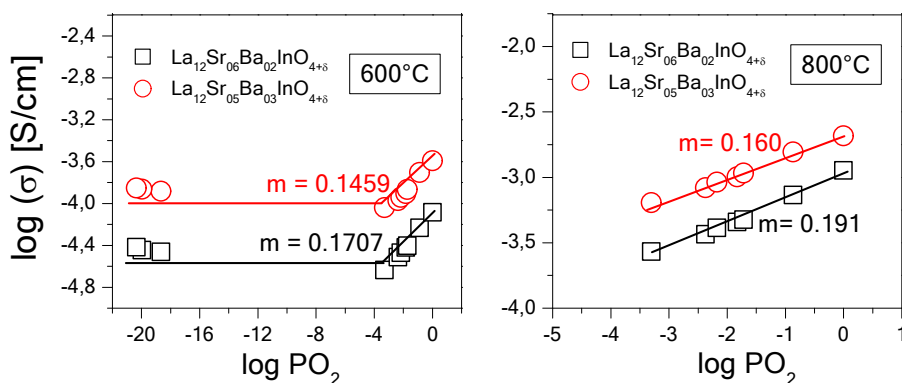

Figure 6. Total electrical conductivity of $La_{1.2}Sr_{0.8-x}Ba_xInO_{4+\delta}$ (x= 0.2, 0.3) vs. oxygen partial pressure, PO_2/atm at 600° and 800°C

At the two temperatures, the slope of the curve (m) is given in Figure 6. The slopes for both compounds at different temperature are near 1/6, which is the expected value for total electrical conductivity when electron holes (p-type conduction) and oxygen vacancies intervene in the conductivity. There are several works that report p-type driving at high pO_2 for solid electrolytes, but, to the best of our knowledge, it had not been reported for layered perovskites [23-28]. The origin of p-type conduction is unclear. Electrons holes and interstitial oxide ions can be created at high oxygen partial pressure by an oxidation reaction [29]

$$\frac{1}{2}O_2(g) + V_i \Leftrightarrow O_i'' + 2h^\bullet$$
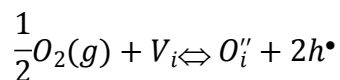
Similar to what happens to other perovskites and Ruddlesden-Popper phases, the electron holes could be located in the B-sites (as in in this case). However, TG measurement in the same condition does not show any detectable weight variation (the oxygen content remains constant in the sample), which is in agreement with the absence of change in the oxidation state of In.

Another possible explanation of why these compounds behave like this, is that at RT water molecules are not only inserted into the interstitial space, but also in oxygen vacancies to form protonic defects, such as $OH_O^{\bullet}$. As temperature increases, the dehydration may cause the formation of oxygen vacancies and/or electron holes. It is expected that although the water content is too low to be detected by TG at 600-800 ºC, the formation of a small quantity of electron holes might be enough to produce a change in the conductivity due to its high mobility compared with ion charge carriers. The obtained conductivities are of the order of $\approx 10^{-4}$ (S/cm), far below the conductivity values of the oxide electrodes used in SOFCs, whose values are greater than 0.1 (S/cm). Also, as we see below, the activation energy, Ea, corresponds to 1 eV, the typical value for ionic conductors. To analyze the nature of the majority charge carriers, ac impedance spectroscopy was applied. The charge transport in this O-ionic conductors takes place through oxygen vacancies as well as interstitial atoms present in the interlayer space, by a "jump" mechanism. The total driving process is affected by three types of resistances: charge transport process in the bulk, charge transport process through the grain boundary and charge transfer process in the material interface – electrode. The typical impedance spectra can be represented in a Nyquist diagram as semi-circles corresponding to each process. The ac impedance spectroscopy between 600 – 900 °C is displayed in Fig. 7 for $La_{1.2}Sr_{0.8-x}Ba_xInO_{4+\delta}$ (x= 0.0, 0.2, 0.3) at different temperatures (600°C, 700°C, 800°C and 900°C).

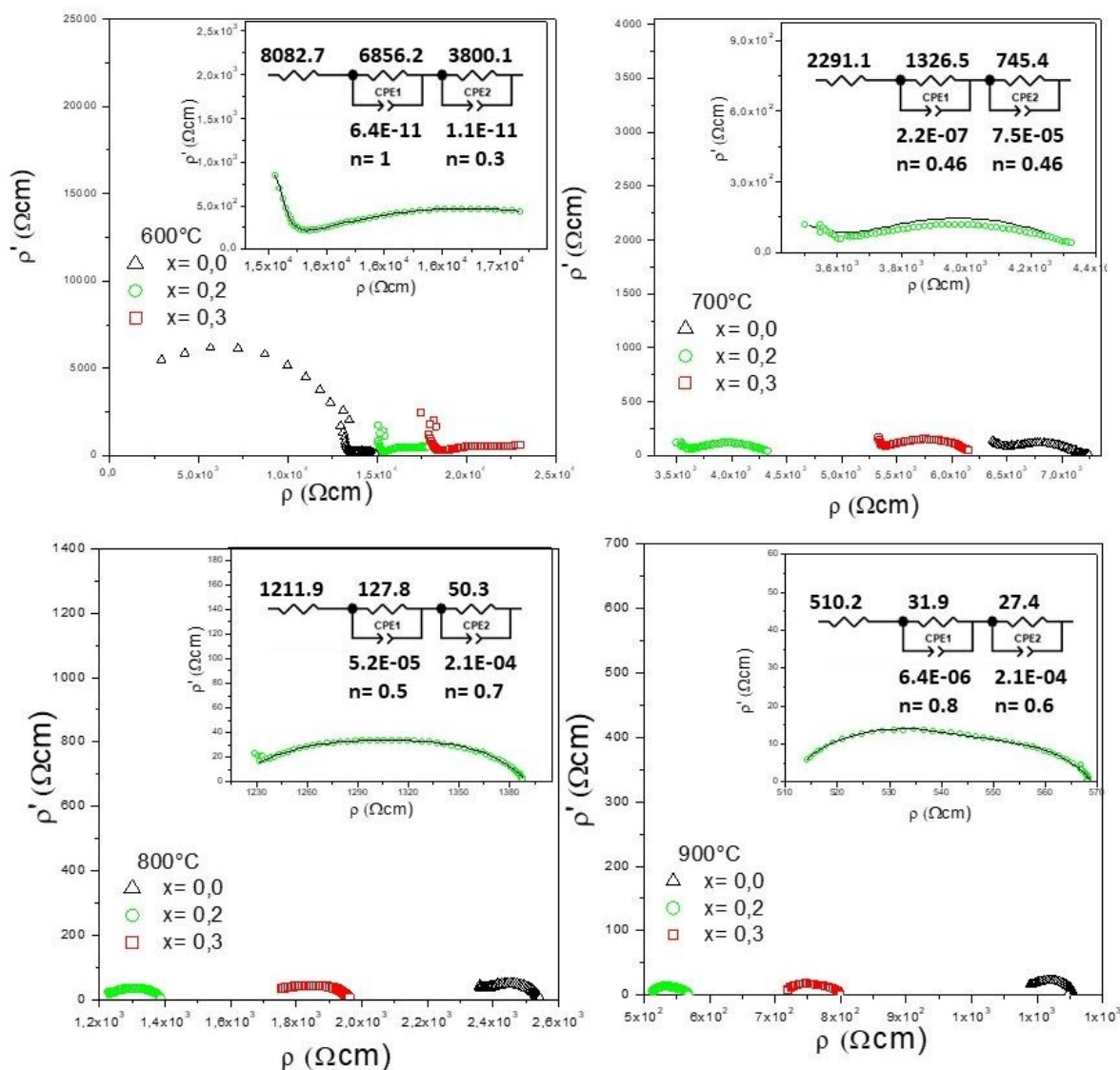**Figure 7.** ac impedance spectra of $La_{1.2}Sr_{0.6}Ba_{0.2}InO_{4+\delta}$ at increasing temperatures with Pt electrodes in air. The determination of the resistances was obtained with two series of RC parallel circuits proposed as the electrical equivalent circuit.

As expected, for the three compounds, the resistances decreased with increasing temperature. The experimental results were adjusted to RC-type circuits as indicated in the inset of the figures. The capacitive contribution is a fundamental factor in the distinction of processes. At high temperatures, between 700-900 °C, it is observed that the resistivity of the $x = 0.2$ and 0.3 compounds decreases with respect to the one with $x = 0.0$, reaching even half of the resistance value for $x = 0.2$. At the temperature of 600 °C, it can be seen that the resistance for $x = 0$ is smaller (lower) than the one of the Ba-containing samples. This is because, as

previously studied [from ref. 15], there is a change in the slope of the activation energy for the x=0 sample, which is not observed in the Ba-containing specimens. For each temperature, the spectrum obtained for the sample with x = 0.2 is observed as an inset. The chosen circuit is a resistance followed by two R-CPE (CPE= constant phase element) circuits in series. We use a CPE because the semicircles are not perfect and in this way the problem can be solved mathematically. The first R represents the resistances given by the bulk + grain boundary, which cannot be observed as a semi-circumference since frequencies greater than 1 MHz would be needed. The reason for representing the spectrum with two circuits of R-CPE type is to account for the two main processes observed in the electrolyte. The first circuit represents the contribution of the charge transfer process in the material interface – electrode. We can infer this from the value obtained for the CPE components, which are typically in the ranges between 10^{-5} and 10^{-6} F. Our values for the first R-CPE are $6.4 \cdot 10^{-6}$ F and $5.2 \cdot 10^{-5}$ F for 900°C and 800°C respectively. The second R-CPE circuit corresponds to the impediment of the oxygen reduction reaction (ORR) at the interface, which was observed in all the spectra. At lower temperature, the resistance of the material depends strongly on temperature, which is a fundamental variable for activating the ionic conduction process. For this reason, when the temperature decreases, the resistances increase, being possible to appreciate the contribution of the resistance of the bulk and the resistance through the grain boundary, as observed at 700°C and 600°C.

The Arrhenius plots (Fig. 8) for $La_{1.2}Sr_{0.8-x}Ba_xInO_{4+\delta}$ (x= 0.0, 0.2, 0.3) show the temperature dependence of the conductivity (σT) in air, where σ is defined as the inverse of the electrical resistivity ρ ($\sigma = 1/\rho$).
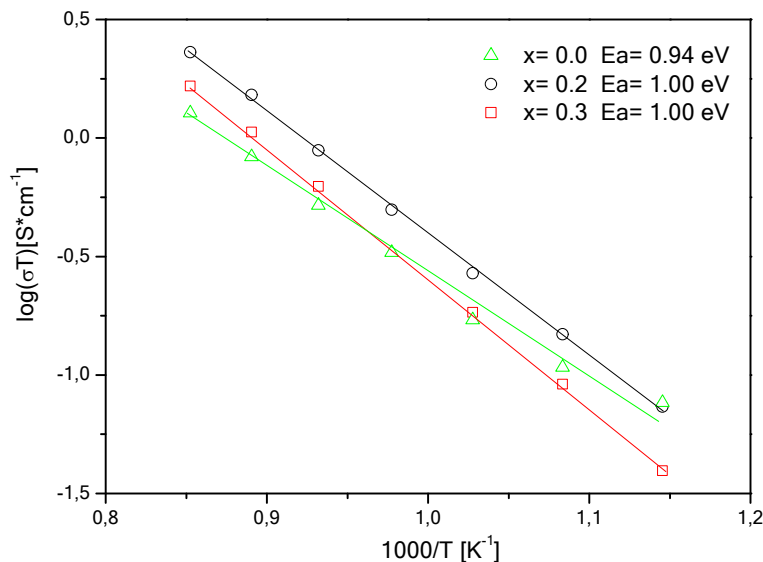
Figure 8. Thermal variation of conductivity (σ) versus 1000/T in air for $La_{1.2}Sr_{0.8-x}Ba_xInO_{4+\delta}$ (x= 0.0, 0.2, 0.3)

From these plots we were able to obtain the activation energy values, Ea, of 1.10 eV for each compound, which are similar to those found for commercial electrolytes and are in agreement with the dc-conductivity measurements described above. In the range between 900°C and 600°C, the x= 0.2 material presents the best values of conductivity, overcoming by a factor of two the conductivity of the parent $La_{1.2}Sr_{0.8}InO_{4+\delta}$ oxide [15]. Therefore, the introduction of Ba in the framework indeed improves the σ values, as wanted. This has a double reason: on the one hand, the notable expansion of the unit-cell volume of the x= 0.2 material (V= 432.42(4) Å^3) with respect to the parent oxide (437.12(9) Å^3) undoubtedly favors oxygen diffusion across the structure. On the other hand, the Ba material was found to present vacancies at axial O2 oxygen atoms besides interstitials, which are the only feature of the parent compound, and seemingly the double mechanism is more effective involving jumps from oxygen interstitials to vacancies. The reason why the Ba-containing compound is more prone to the existence of vacancies is uncertain, although it can be related to the lower covalence of the chemical bonding of axial oxygens with the NaCl layer, increasing the lability of O2 atoms in $La_{1.2}Sr_{0.6}Ba_2InO_{4+\delta}$.

Conclusions

We found a double functionality in the novel $La_{1.2}Sr_{0.6}Ba_2InO_{4+\delta}$ oxide. This compound is able to incorporate and dissociate water molecules in the interstitial space, taken from the ambient atmosphere during the cooling process from the synthesis temperature of 1300ºC. This could be of application in thermochemical water splitting. Difference Fourier maps from NPD data at RT clearly show conspicuous negative peaks corresponding to hydrogen atoms; H1 and H2 atoms are bonded at about 1 Å to O3 interstitial oxygen and O2 axial oxygen from the octahedral layer, respectively. H_2O molecules do not alter the electroneutrality of the crystal, and at higher temperatures (600 and 800ºC) they are no longer observed, remaining the interstitial oxygen atoms corresponding to the charge misbalance of the metal ions. Unlike in the parent $La_{1.2}Sr_{0.8}InO_{4+\delta}$ oxide, these interstitials are combined with a noticeable number of O2 vacancies. The dual observed defects, vacancies and interstitials, are effective in increasing the conductivity of the Ba-containing material in the 600-900ºC temperature range. This strategy seems operative for the design of novel and functional oxide-ion conductors to operate in SOFCs at intermediate temperatures.

Conflicts of interest

There are no conflicts of interest to declare

Acknowledgments

References

[1] A. L. Facci, V. Cigolotti, E. Jannelli, S. Ubertini, *Applied Energy*, 2017, **192**, 563-574,

[2] A. Weber, E. Ivers-Tiffée, *Journal of Power Sources*, 2004, **27**, 273-283

[3] S.P.S. Badwal, *Solid State Ionics*, 1992, **52**, 23-32

[4] B.C.H. Steele, *Solid State Ionics*, 2000, **129**, 95-110

[5] K. Huang, R. S. Tichy, J. B. Goodenough, *J Am Ceram Soc*, 1998. DOI: 10.1111/j.1151-2916.1998.tb02662.x

[6] S. Lee, X. Guan, *MRS Communications*, 2017, **7**, 199-205

[7] A. Aguadero, J. A. Alonso, M. T. Fernandez-Diaz, M. J. Escudero, L. Daza, *J. Power Sources*, 2007, **169**, 17-24.

[8] G.N. Mazo, S.M. Kazakov, L.M. Kolchina, A.V. Morozov, S.Ya. Istomin, N.V. Lyskov, A.A. Gippius, E.V. Antipov, *J. Alloys Compd.*, 2015, **639**, 381-386

[9] F. Zhao, X. Wang, Z. Wang, R. Peng, C. Xia, *Solid State Ionics*, 2008, **179**, 1450-1453

[10] T. Nakamura, Y. Ling, K. Amezawa, *J. Mater. Chem. A,* 2015 ,**3**,10471-10479

[11] K. Kawamura, M. Yashima, K. Fujii, K Omoto, K. Hibino, S. Yamada, JR Hester, M Avdeev, P Miao, S Torii, T Kamiyama, *Inorg. Chem.*, 2015, **54**, 3896–3904

[12] K.W. Hyung, T.Y. Kwon, Y. Jeon, *Solid State Communications*, 2003, **125**, 259-264

[13] S. J. Skinner, J. A. Kilner, *Materials Today*, 2003, **6**, 30-37

[14] L. Troncoso, J. A. Alonso, M.T. Fernández-Díaz, A. Aguadero, *Solid State Ionics*, 2015 **282**, 82–87

[15] L. Troncoso, J. A. Alonso, A. Aguadero, *J. Mater. Chem. A*, 2015, **3**, 17797–17803

[16] H.M. Rietveld, *J. Appl. Crystallogr.* 1969, **2,** 65–71

[17] J. Rodríguez-Carvajal, *Physica B*, 1993, **192,** 55–69.

[18] D. Johnson, Zview Program, version 3.2b, Scribner Associates, Inc., Southern Pines, North Carolina, 1990–2010.

[19] A. Caneiro, P. Bavdaz, J. Fouletier, J. P. Abriata, *Rev. Sci. Instrum.*, 1982, **53,** 1072.

[20] Yu. A. Titov, N.M. Belyavina, V.Ya. Markiv, M.S. Slobodyanik, Ya.A. Krayevska, *Dopov. Nats. Akad. Nauk. Ukr.*, 2009, **10,** 160-166

[21] M. Orfila, M. Linares, R. Molina, J.A. Botas, R. Sanz, J. Marugán, *Int J Hydrogen Energy*, 2016, **41**, 19329-19338

[22] L. Wang, M. Al-Mamun, P. Liu, Y. Wang, H. G. Yang, H. Zhao, *Journal of Materials Science*, 2018, **53**, 6796–6806

[23] Kharton, V.V., Yaremchenko, A.A., Viskup, A.P. et al. *Ionics*, 2002, **8**, 215-222

[24] V.V.Kharton, F.M.B.Marques, A.Atkinson, *Solid State Ionics*, 2004, **174**, 135-149

[25] A.Manthiram, J.F.Kuo, J.B.Goodenough, *Solid State Ionics*, 1993, **62**, 225-234

[26] Tatsumi Ishihara, Hideaki Matsuda, YusakuTakita, *Solid State Ionics*, 1995, **79**, 147-151

[27] Jin-Ho, Kim Han-Il Yoo, *Solid State Ionics*, 2001, **140**, 105-113

[28] T. Takahashi, H. Iwahara, *Energy Conversion*, 1971, **11**, 105-111

[29] P. Knauth, M. L. Di Vona, Solid State Proton Conductors: Properties and Applications in Fuel Cells, John Wiley & Sons, 2012